Journal of Applied Fluid Mechanics, Vol. 17, No. 9, pp. 1967-1980, 2024.
Available online at www.jafmonline.net, ISSN 1735-3572, EISSN 1735-3645.
https://doi.org/10.47176/jafm.17.9.2600

Numerical Analysis of Mechanism on Heat Transfer Deterioration of Hexamethyldisiloxane in a Vertical Upward Tube at Supercritical Pressures

J. Fu[1,2†], H. Y. Liu[1,2] and Y. Wang[1]

[1] *College of Energy and Power Engineering, Lanzhou University of Technology, Lanzhou, Gansu, 730050, China*
[2] *Collaborative Innovation Center for Supporting Technology of Northwest Low-Carbon Towns, Lanzhou, Gansu, 730050, China*

†Corresponding Author Email: fujian@lut.edu.cn

ABSTRACT

The working fluids at supercritical pressures will experience abnormal heat transfer compared with those in a sub-critical state. In particular, the heat transfer deterioration (HTD) can make the wall temperature increase sharply in the tube, posing a challenge for the design of heat exchangers in the supercritical organic Rankine cycle (SORC). It is generally acknowledged that the effects of buoyancy and flow acceleration lead to abnormal heat transfer. However, a clear understanding of the interactions between the turbulent flow and heat transfer characteristics still needs to be further improved by obtaining the internal flow mechanism. The current study analyses the contours of the turbulent flow information under the different boundary conditions by means of validated CFD numerical simulation based on the previous experimental data and reveals the main causes of HTD and the impact mechanism of boundary conditions. The results reveal that two deteriorated extreme points are generated in a vertical upward tube with uniform heat flux for hexamethyldisiloxane at supercritical pressures. The buoyancy and flow acceleration effects caused by the drastic variation in fluid density near the pseudo-critical temperature can deform the velocity profile, thus reducing the local shear stress and turbulence intensity, and leading to the HTD. Moreover, HTD gets worse with the increase in heat flux and moderate with the rise in supercritical pressure. This study should support the data and theory for the refined design of heaters applied to the SORC in the future.

Article History

Received January 18, 2024
Revised March 28, 2024
Accepted April 8, 2024
Available online July 2, 2024

Keywords:

Numerical simulation
Hexamethyldisiloxane
Supercritical pressure
Vertical upward flow
Heat transfer deterioration

1. INTRODUCTION

In the fields of thermoelectric conversion technology for the recovery and utilization of industrial waste heat, the organic Rankine cycle has the characteristics of a wide applied range of heat source temperature, high steam pressure, simple system composition and flexible installed capacity, among others, which can convert low-grade thermal energy into high-grade mechanical energy (Lecompte et al., 2015; Loni et al., 2020). As the critical parameters of organic working fluids are generally low, it is easy to reach a supercritical state, thus forming a supercritical organic Rankine cycle (SORC), which can effectively elude the gas–liquid phase area in the sub-critical cycle, and decrease the exergy loss caused by the latent heat of evaporation and the deterioration of heat transfer that arises from the superheated boiling (Yağli et al., 2016). As a working fluid, hexamethyldisiloxane (MM) has the advantages of a relatively low critical point (T_c = 518.75 K, P_c = 1.939 MPa), excellent thermal stability, and a moderate boiling point, among others, which make it substantially suitable for the SORC with medium- and high-temperature heat sources (Lai et al., 2011; Dai et al., 2019).

Compared with the characteristics of heat transfer with subcritical fluids in the tube, there are three kinds of heat transfer states for supercritical fluids: heat transfer normal, heat transfer enhancement (HTE) and heat transfer deterioration (HTD) (Cabeza et al., 2017; Nieuwenhuyse et al., 2023). By summarizing the heat transfer characteristics of water at supercritical pressures, Pioro (2019) concluded that the water with supercritical pressures would gradually convert HTE to HTD with the increase in heat flux, when the pressure and mass flux were constant. Due to the sharp increase of the specific heat near the critical point, an extreme value of enhanced

NOMENCLATURE

A	sectional area
c_p	specific heat
d	diameter of tube
G	mass flux
g	acceleration of gravity
H	enthalpy
h	heat transfer coefficient
I	turbulence intensity
k	turbulent kinetic energy
P	pressure
q	heat flux
r	radius of tube
T	temperature
u	velocity
u'	fluctuating velocity
$\overline{U}$	time-average velocity
x	axial direction
y	radial direction
y^+	radial dimensionless distance
Greek symbols	
δ	thickness of flow boundary layer
ε	turbulent dissipation rate
λ	thermal conductivity
μ	dynamic viscosity
ρ	density
τ	shear stress
ω	specific dissipation rate
Subscripts	
b	bulk
c	critical point
$D–B$	Dittus–Boelter correlation
exp	experimental data
f	fluid
in	inlet
lam	laminar
m	mean value
num	numerical data
pc	pseudo-critical
tur	turbulent
w	wall
Abbreviations and acronyms	
2D	two-dimensional
CFD	Computational Fluid Dynamics
EWT	Enhanced Wall Treatment
HTD	Heat Transfer Deterioration
HTE	Heat Transfer Enhancement
RANS	Reynolds Average Navier-Stokes
SO	Stress-Omega

heat transfer near the pseudo-critical point will be produced according to the Dittus–Boelter correlation. The HTE phenomenon can be found in many studies on supercritical heat transfer (Mao et al., 2021). However, the specific heat is not the only factor affecting the heat transfer coefficient, and there are other factors such as the effects of buoyancy and flow acceleration caused by density change (Pizzarelli, 2018), so the heat transfer coefficient near the pseudo-critical point will deviate from the calculated values by the Dittus–Boelter correlation. In general, heat transfer will be enhanced as the heat flux is lower, and reduced significantly when the heat flux is higher (Huang et al., 2016). Cheng and Schulenberg (2001) concluded that HTD only occurred in the range of $T_b < T_{pc} < T_w$ under a higher heat flux with a lower mass flux.

HTD will cause the local temperature of the inner wall to surge in the tube (Zhu et al., 2019). Once it exceeds the pyrolysis temperature of the organic working fluids in the heat exchanger of SORC, the working fluids will not only decompose the compounds that may be corrosive, toxic and flammable, but also form solid particles which deposit on the surface of the heater and turbine (Gallarini et al., 2023). Moreover, the outlet temperature of the heater in SORC will also decrease with the pyrolysis of the working fluids, resulting in the cyclic working fluids failing to reach the supercritical state (Wang et al., 2022). These consequences can deteriorate the performance of the overall system. Essential components can even be damaged. It puts forward a challenge for the design of heat exchange equipment. Therefore, HTD for fluids at supercritical pressures has received relatively more attention from researchers.

Ackerman (1970) studied the heat transfer characteristics of water at supercritical pressures in the vertical tubes and attributed the HTD observed in $T_b < T_{pc} < T_w$ to a pseudo-film-boiling process similar to film boiling occurring at sub-critical pressures. Xu et al. (2020a) and Zhu et al. (2020) noted that the fluids in the trans-critical state are a pseudo-boiling phenomenon, and HTD in the tubes is similar to the boiling of the nucleate under the sub-critical pressure. Jackson et al. (1989) concluded that the HTD of fluids with supercritical pressures under low mass flux conditions was attributed to the action of buoyancy through experimental and theoretical analysis. The buoyancy is due to the uneven fluid density with the gravity, which will deform the profile of fluid velocity and shear stress. The heat transfer is affected sequentially. McEligot et al. (1970) found that the flow in a heating tube with high heat flux would produce an effect of acceleration due to the decline of density in the axial direction through the experiment, which could contribute to the flow transition from turbulent to laminar and lead to the inner wall temperature increasing. He et al. (2005) found that the buoyancy effect was not evident in the micro-tube through numerically investigating the heat transfer characteristics of supercritical CO_2 in a vertical tube with a diameter of 0.948 mm, and the flow acceleration effect under the intense heating conditions would weaken the turbulence correspondingly, thus the heat transfer was significantly damaged. Kim & Kim(2011) revealed that the influence of buoyancy was weak in a vertical tube with a diameter of 4.5 mm for the heat transfer characteristics of supercritical CO_2, whereas the effect of flow acceleration resulted in the HTD. However, it is generally believed that the HTD in the vertical tubes of fluids with supercritical pressures attributes to the coupling effects of buoyancy and flow acceleration in most cases (Mikielewicz et al., 2002; Kim & Kim, 2010; Jackson, 2017; Liu et al., 2017).

The characteristics of convective heat transfer are closely related to the internal flow state of the working

fluids, and it is most commonly necessary to use advanced visualization means and related testing techniques to obtain key information about heat transfer and clarify its mechanism (Yang et al., 2015). However, because the pressure and temperature of supercritical fluids are relatively high, the implementation of relevant visualization experiments is extremely tough and costly (Yoo, 2013). The numerical simulation method with computational fluid dynamics (CFD) is easy to operate and low in cost. The method can provide a large amount of internal flow information on convective heat transfer in the tube and special-shaped channels (Tu & Zeng, 2021; Liu et al., 2023; Hou et al., 2024) to explore the mechanism of the heat transfer, and especially exploit lots of new study ideas for HTD. Mohseni and Bazargan (2012) studied the supercritical CO_2 with vertical flow in a tube by CFD with a two-dimensional model and discovered that the third mechanism is turbulent viscosity affecting HTD, apart from the buoyancy and flow acceleration effects induced by density variation. The results indicated that the decrease in fluid density near the wall would give rise to a reduction in turbulent viscosity, which could diminish turbulent diffusion and weaken turbulence intensity, ultimately resulting in HTD. Lei et al. (2016) simulated the heat transfer of supercritical CO_2 in the vertical tube by using a two-dimensional model and observed the two-peak wall temperature. Since this phenomenon only occurs under the conditions of high q/G, it is difficult to measure experimentally. It was found that both fluid velocity and kinetic energy are lower near the wall region as the HTD occurred. Li et al. (2024) implemented CFD on the heat transfer of supercritical CO_2 in a horizontal tube and summarized that the near-wall area was occupied by the high specific heat of fluid at low q/G, and absorb lots of heat, thus contributing to HTE. At high q/G, the high specific heat was away from the wall gradually, and the effect of buoyancy caused by the large density gradient started to appear. The heat transfer was impaired.

In summary, in order to clearly illustrate the heat transfer mechanism of MM in a vertical upward tube at supercritical pressures, the in-tube and near-wall distributions of key parameters affecting convective heat transfer under the different boundary conditions through the CFD numerical simulation are analyzed in the present study. Combined with the relevant experimental data, the main mechanism of the abnormal heat transfer phenomenon and the influence of boundary conditions such as heat flux and pressure on it are revealed.

2. NUMERICAL METHODS AND DATA PROCESSING

2.1 Numerical Methods

The simulated model is an 830 mm long vertical upward tube with an inner diameter of 2.4 mm, whose geometric size is in accordance with the existing test rig based on the compact heat exchanger of SORC (Xu et al., 2020b). To reduce the computational cost of numerical simulation on the convective heat transfer in the vertical circular tubes, a 2D axisymmetric structure model is employed, as shown in Fig. 1(a). The modeling, meshing

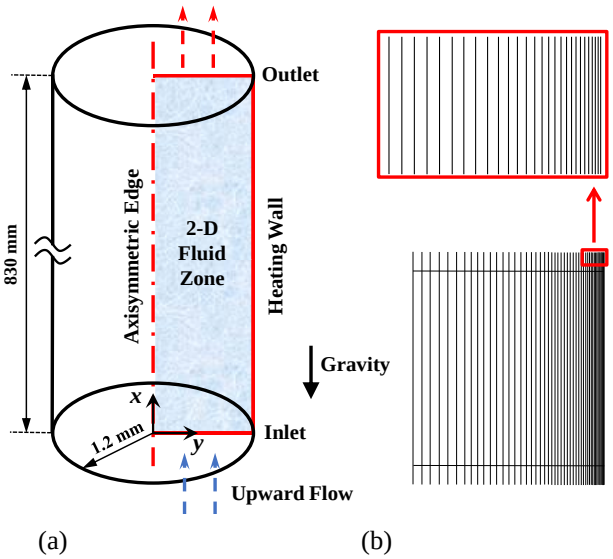

Fig. 1 Schematic of simulated model: (a) geometric dimensioning; (b) near-wall grid

and boundary condition setting are implemented by Gambit 2.4.6. The whole model is set to be a fluid domain without regard to the wall thickness. The upper and lower boundaries are set as the pressure outlet and the mass flow inlet, respectively. The left side is the axisymmetric boundary, and the right side is the heating wall with the constant heat flux. The tube wall is defined as a no-slip wall with a roughness of 0.5. Considering that the variation gradient of fluid thermo-physical parameters near the wall is large, the mesh is refined, as shown in Fig. 1(b). Since the grid height of the first layer from the wall is set at 0.001 mm, y^+ of the wall is calculated to be between 0.18 and 0.61 accordingly.

To avoid the influence of the grid quantity on the accuracy of calculated results, it is needed to validate the grid-independent solution of the numerical model. In the present study, the grid quantity is changed by adjusting the axial elements (x direction) and radial elements (y direction), and then the effects of the grid quantity on the calculated results are evaluated by the comparison of the wall temperature. The results demonstrate that when the radial elements are constant and the axial elements are increased from 830 to 1,660, the wall temperature is almost unchanged, as shown in Fig. 2. While the radial elements are refined from 50 to 200 under the axial elements of 830, the maximum errors of the wall temperature are reduced from 0.89% to 0.13% compared with those with the radial elements of 400. Notably, the radial elements are refined to 200, the impact on the wall temperature is already small, so the grid quantity of the numerical model is finally selected as 166,000 (830 × 200) cells (Xu et al., 2022).

The CFD software Fluent (2022R1) is used to perform the numerical simulation on the convection heat transfer of MM with the steady-state in a vertical upward tube at supercritical pressures. The gravitational acceleration is set at −9.81 m/s^2 in the axial direction, which is opposite direction of the flow. The thermos-physical properties of MM can be queried by NIST REFPROP 9.1 and enter

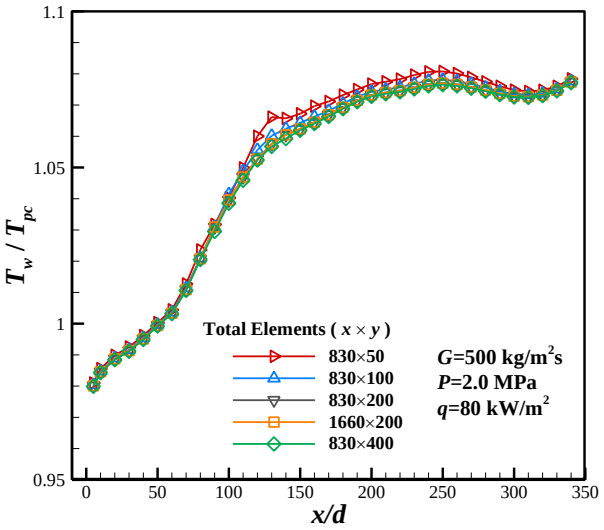

Fig. 2 Analysis of grid independence from the wall temperature

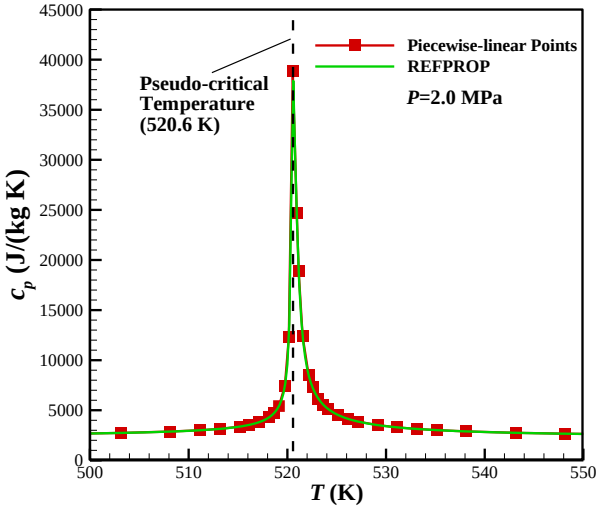

Fig. 3 Piecewise-linear points of specific heat

them into Fluent through the piecewise-linear method. Figure 3 shows the piecewise-linear points of specific heat compare with all points from REFPROP. It can be seen that the piecewise-linear points well describe the dramatic change of specific heat near T_{pc}. Compared with the curve of specific heat obtained from REFPROP, the maximum error is 2.43%. Other Settings in Fluent can be found in Table 1.

The simulated conditions are consistent with our previous experimental study (Xu et al., 2020b). The inlet mass flux is 500 kg/m^{2}s, and the operating pressure is 2.0 and 2.4 MPa. The heating edge of the tube is implemented with an approximately constant heat flux of 80 and 100 kW/m^2. The reason why the heat flux is not an absolute constant is that the nonlinear wall temperature caused by the abnormal heat transfer will make the resistivity and heat loss of the testing tube distribute nonuniformly. As shown in Fig. 4, under the experimental condition that the mass flux is 500 kg/m^{2}s, the pressure is 2.0 MPa and the heat flux is 80 kW/m^2, the measured minimum heat flux is

Table 1 Numerical parameters

Setting Items	Parameters
Roughness of wall	0.5
Grid height of the first layer	0.001 mm
y^+	0.18 ~ 0.61
Total grids	166,000 (830 × 200)
Gravity value	-9.81 m/s^2
Solution method	
Pressure-velocity coupling	SIMPLEC scheme
Gradient	Least squares cell based
Pressure	Second order
Momentum	Second order upwind
Turbulent kinetic energy	
Specific dissipation rate	
Energy	
Root mean square residuals	10^{-8}
Turbulent Prandtl number	0.85
Turbulent Schmidt number	0.7
Boundary conditions	
Mass flux	500 kg/m^{2}s
Heat flux	80 and 100 kW/m^2
Pressure	2.0 and 2.4 MPa

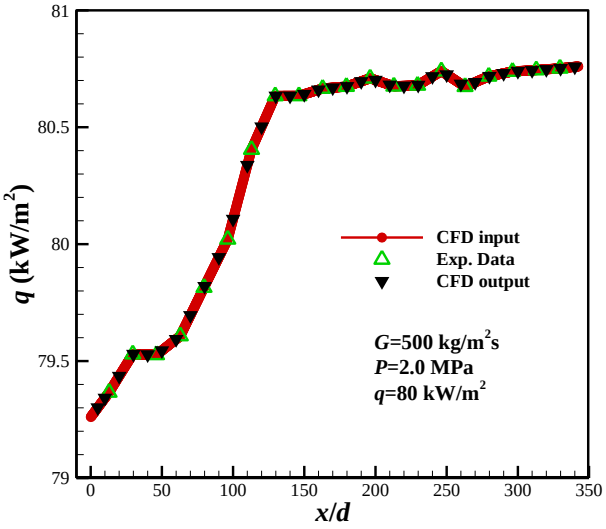

Fig. 4 Input the effective heat flux in the CFD

79.37 kW/m^2, and the maximum heat flux is 80.75 kW/m^2. Its maximum difference from the specified value of 80 kW/m^2 is 0.94%, and the distribution along the axial direction of the tube does not increase or decrease uniformly. On the basis of the 20 tested points, the heat flux distributions on the 830 numerical nodes are obtained by linear interpolation, and then input into Fluent software through a custom file. It can be ensured that the output heat flux values in the CFD data processing are exactly the same as the ones in the experiment.

2.2 Governing Equations

The fundamental governing equations for 2D axisymmetric model in the cylindrical coordinates, as follows:

Continuity:

$$\frac{1}{y}\left[\frac{\partial}{\partial x}(y\rho u)+\frac{\partial}{\partial y}(y\rho v)\right]=0 \tag{1}$$

Axial Momentum:

$$\frac{1}{y}\left[\frac{\partial}{\partial x}(y\rho u^2)+\frac{\partial}{\partial y}(y\rho vu)\right]=-\frac{\partial P}{\partial x}+\rho g +\frac{1}{y}\left\{2\frac{\partial}{\partial x}\left[y\mu_e\left(\frac{\partial u}{\partial x}\right)\right]+\frac{\partial}{\partial y}\left[y\mu_e\left(\frac{\partial u}{\partial y}+\frac{\partial v}{\partial x}\right)\right]\right\} \tag{2}$$

Radial Momentum:

$$\frac{1}{y}\left[\frac{\partial}{\partial x}(y\rho uv)+\frac{\partial}{\partial y}(y\rho v^2)\right]=-\frac{\partial P}{\partial y}-2\frac{\mu_e v}{y^2} +\frac{1}{y}\left\{\frac{\partial}{\partial x}\left[y\mu_e\left(\frac{\partial v}{\partial x}+\frac{\partial u}{\partial y}\right)\right]+2\frac{\partial}{\partial y}\left[y\mu_e\left(\frac{\partial v}{\partial y}\right)\right]\right\} \tag{3}$$

Energy:

$$\frac{1}{y}\left[\frac{\partial}{\partial x}(y\rho uh)+\frac{\partial}{\partial y}(y\rho vh)\right] =\frac{1}{y}\left\{\frac{\partial}{\partial x}\left[y\left(\frac{\mu}{Pr}+\frac{\mu_t}{Pr_t}\right)\frac{\partial h}{\partial x}\right]+\frac{\partial}{\partial y}\left[y\left(\frac{\mu}{Pr}+\frac{\mu_t}{Pr_t}\right)\frac{\partial h}{\partial y}\right]\right\} \tag{4}$$

where x is the axial direction, y is the radial direction, u is the velocity in the axial direction, and v is the velocity in the radial direction, μ_e is the effective viscosity defined by $\mu_e=\mu+\mu_t$, μ is the fluid viscosity, μ_t is the turbulent viscosity, h is the fluid enthalpy, Pr is the fluid Prandtl number, Pr_t is the turbulent Prandtl number. In the present study, Pr_t is the default value of 0.85.

2.3 Data Processing

The local Nusselt number characterizing the heat transfer characteristics along the tube is defined as follows:

$$Nu_x=\frac{h_x d}{\lambda_x} \tag{5}$$

where d is the inner diameter of the tube and λ_x is the local thermal conductivity. h_x is the local convection heat transfer coefficient and is defined as follows:

$$h_x=\frac{q_x}{T_{w,x}-T_{b,x}} \tag{6}$$

q_x is the wall heat flux and its input values are coincident with the experimental data. A specific processing method has been introduced in Fig. 4. $T_{w,x}$ is the local wall temperature, and its corresponding values can be obtained in Fluent. $T_{b,x}$ is the local average fluid temperature in the tube. Since the fluid temperature is not evenly distributed on the cross-section, the following equation is usually used in convection heat transfer to define the average fluid temperature on the section, known as the bulk temperature (Holman, 2010):

$$T_b=\frac{\sum_{i=1}^{n} c_{pi}\cdot T_i\cdot\rho_i\left|\overline{u_i}\cdot\overline{A_i}\right|}{\sum_{i=1}^{n} c_{pi}\cdot\rho_i\left|\overline{u_i}\cdot\overline{A_i}\right|} \tag{7}$$

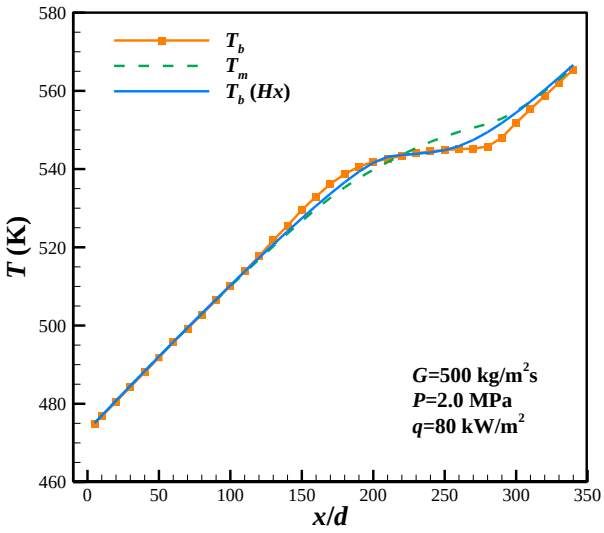

Fig. 5 Results on bulk temperature under different calculated methods

whereas the mass-weighted average temperature is generally adopted to conduct the average temperature in the software, which is defined as follows:

$$T_m=\frac{\sum_{i=1}^{n} T_i\cdot\rho_i\left|\overline{u_i}\cdot\overline{A_i}\right|}{\sum_{i=1}^{n}\rho_i\left|\overline{u_i}\cdot\overline{A_i}\right|} \tag{8}$$

If the specific heat is constant or its variation is small, the average fluid temperature calculated by the above two equations can be considered to be approximate. However, the specific heat will change dramatically when the fluid temperature reaches T_{pc} at the supercritical pressures, resulting in deviations from the average fluid temperature obtained by the two methods near the T_{pc} area. Taking the condition with a mass flux of 500 kg/m^{2}s, a pressure of 2.0 MPa and a heat flux of 80 kW/m^2 as an example, as shown in Fig. 5, the defined fluid average temperature (Eq. (7)) and the mass-weighted fluid average temperature (Eq. (8)) exhibit an apparent difference near T_{pc} ($x/d \approx 220$, T_{pc} = 520.55 K). The maximum deviation of 1.11% occurs in the region after T_{pc}, of which the absolute value is 5.82 K. By contrast, in the region far from T_{pc}, the average fluid temperature calculated by the above two methods is basically the same.

In addition, the fluid temperature (T_b (H_x)) obtained by the energy conservation method applied to the experiment is shown in Fig. 5, which is to use the fixed correspondence between temperature and enthalpy of the fluid under the determined pressure to calculate the local enthalpy value through the one-dimensional energy conservation principle in the tube to obtain the average fluid temperature at the corresponding position (Xu et al., 2020b). It can be observed that the fluid temperature obtained by the energy conservation method is between the above two calculated fluid temperatures, and the maximum deviation from the defined average fluid temperature is 0.71% (the absolute value is 3.73 K).

According to Eq. (5), the thermal conductivity of the working fluid is also the key parameter in calculating the

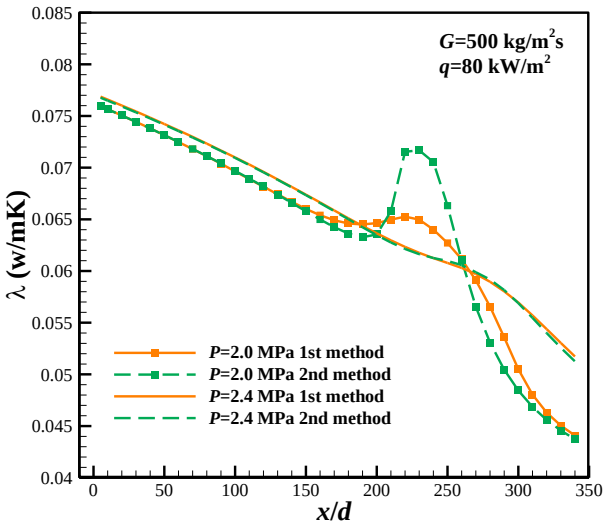

Fig. 6 Results on the thermal conductivity of the working fluid under different calculated methods

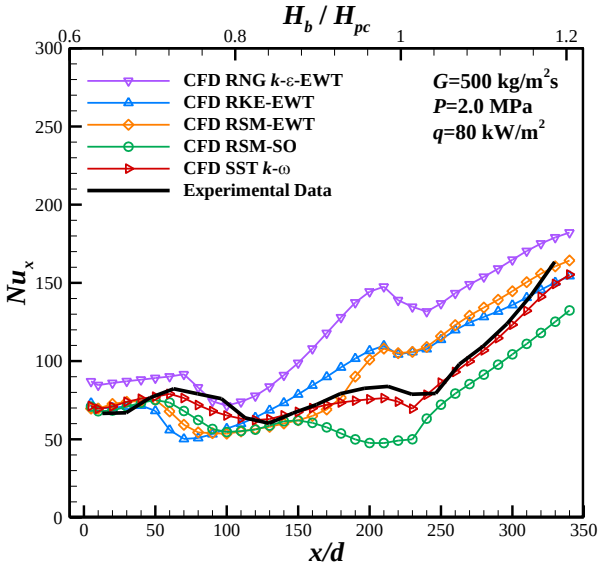

Fig. 7 Validation on turbulence models

Nusselt number. The one-dimensional axial distributions on the thermal conductivity along the tube obtained by the two methods are shown in Fig. 6. The first method is based on the mass-weighted average method in Fluent, as shown by the following equation:

$$\lambda = \frac{\sum_{i=1}^{n} \lambda_i \cdot \rho_i \left|\overrightarrow{u_i} \cdot \overrightarrow{A_i}\right|}{\sum_{i=1}^{n} \rho_i \left|\overrightarrow{u_i} \cdot \overrightarrow{A_i}\right|} \tag{9}$$

The section is established along the axial direction in the simulated model successively, and then the mass-weighted average of the thermal properties at the corresponding positions is calculated. The second method is to calculate the defined average fluid temperature $T_{b,x}$ on the section first, and then check the corresponding thermal properties out through the REFPROP 9.1 software. As shown in Fig. 6, when the pressure is 2.0 MPa, the thermal conductivity calculated by the two methods varies greatly near T_{pc}. While the pressure rises to 2.4 MPa, the thermal conductivity obtained by the two methods is almost the same. Considering experimental data processing (Xu et al., 2020b), the second method is adopted to obtain the thermal properties of the working fluid and calculate the Nusselt number. It can be better to compare the numerical results with the experimental data.

2.4 Validation on Turbulence Models

The application of the turbulence models is of key significance to the calculation results in CFD simulation. The convergent results on the Reynolds Average Navier–Stokes equation (RANS) turbulence model for simulating the in-tube convection heat transfer of MM at supercritical pressures are shown in Fig. 7, including the RNG k–ε with Enhanced Wall Treatment (EWT) model, the realizable k–ε (RKE) EWT model, the Reynolds Stress Model (RSM) EWT model, the RSM with Stress Omega model and the Shear Stress Transport (SST) k–ω model (Menter, 1994). It can be seen that the calculated results of RANS turbulence models are in good agreement with the experimental data near the entrance region except for that of the RNG k–ε EWT model, which may indicate that the working fluid in this region is still completely in a sub-critical state. Moreover, the trend on heat transfer appearing in two deteriorated regions along the flow direction can be predicted by all of the selected RANS turbulence models, but only the result of the SST k–ω turbulence model is well conformed to the experimental data on the whole. The maximum deviation does not exceed 11.7%. Conversely, the results of other RANS turbulence models successively deviate from the experimental values after $x/d \approx 40$. Therefore, the SST k–ω turbulence model is applied to simulate the heat transfer of MM in the vertical upward tube at supercritical pressures in this study.

In the transport equations for SST k–ω turbulence model, the turbulent kinetic energy (k) and the specific dissipation rate (ω) in the cylindrical coordinates are obtained by the following equations, respectively:

$$\frac{\partial}{\partial x}(\rho k u) + \frac{\partial}{\partial y}(\rho k v) = \frac{\partial}{\partial x}\left[\left(\mu + \frac{\mu_t}{\sigma_k}\right)\frac{\partial k}{\partial x}\right] + \frac{\partial}{\partial y}\left[\left(\mu + \frac{\mu_t}{\sigma_k}\right)\frac{\partial k}{\partial y}\right] + G_k - Y_k \tag{10}$$

$$\frac{\partial}{\partial x}(\rho \omega u) + \frac{\partial}{\partial r}(\rho \omega v) = \frac{\partial}{\partial x}\left[\left(\mu + \frac{\mu_t}{\sigma_\omega}\right)\frac{\partial \omega}{\partial x}\right] + \frac{\partial}{\partial r}\left[\left(\mu + \frac{\mu_t}{\sigma_\omega}\right)\frac{\partial \omega}{\partial r}\right] + G_\omega - Y_\omega + D_\omega \tag{11}$$

where σ_k and σ_ω is the turbulent Prandtl numbers for k and ω, respectively, G_k is the production of k, G_ω is the generation of ω, Y_k denotes the dissipation rate of k, Y_ω is the dissipation rate of ω, and D_ω is the cross-diffusion term, of which specific values and calculation methods can be referred to the literature (Menter, 1994).

3. RESULTS AND DISCUSSION

The numerical and experimental results of heat transfer characteristics under the condition of a mass flux

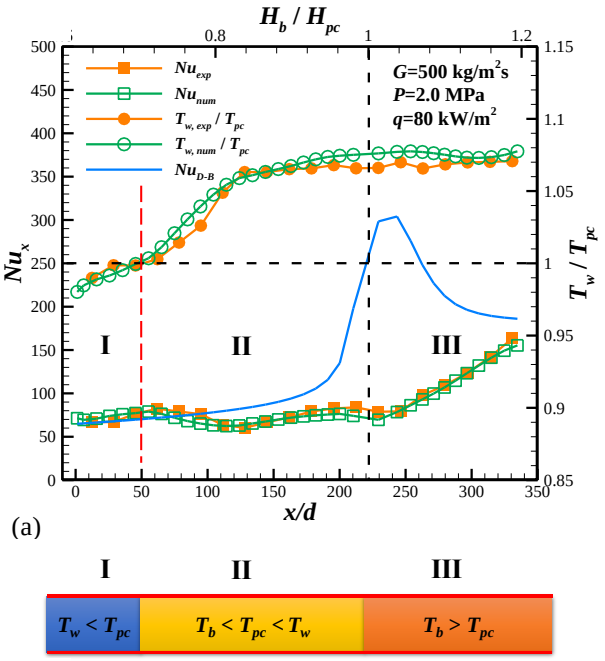

Fig. 8 Heat transfer characteristics: (a) local wall temperature and Nusselt number; (b) temperature division in the heating tube

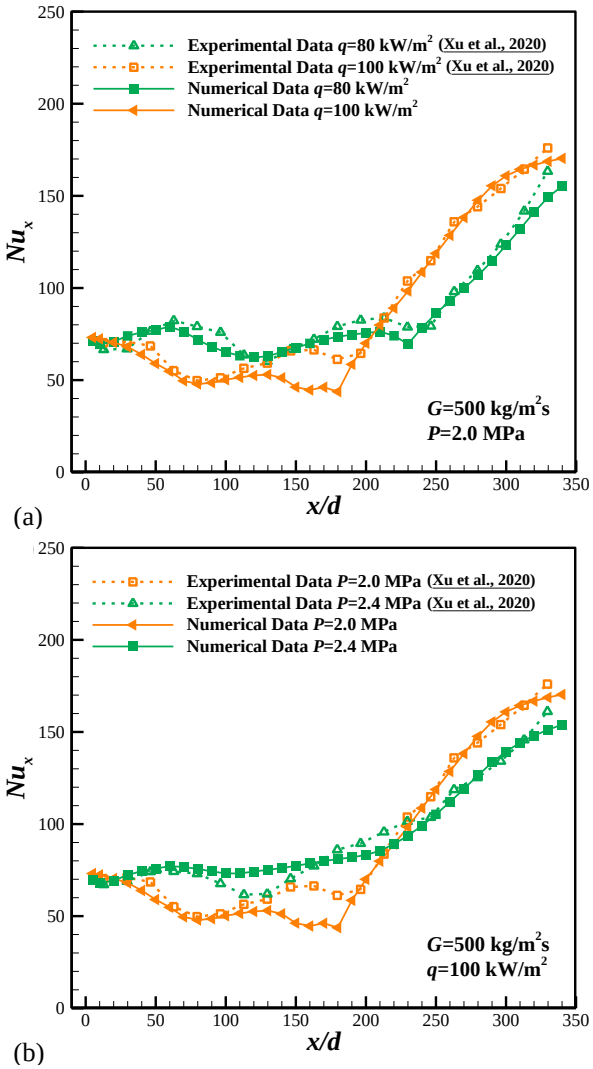

Fig. 9 Effects of boundary conditions on the heat transfer characteristics: (a) effect of heat flux; (b) effect of pressure

of 500 kg/m^{2}s, a pressure of 2.0 MPa and a heat flux of 80 kW/m^2 are shown in Fig. 8(a). It can be seen that the local wall temperature and Nusselt number simulated by Fluent are basically consistent with those of experiment. The maximum deviations for T_w and Nu are 1.29% and 11.7%, respectively. Compared with the normal heat transfer values calculated by the Dittus–Boelter correlation (Holman, 2010), the heat transfer characteristics of MM in the vertical upward tube at supercritical pressures have not been noticeably enhanced; on the contrary, most of them are in a deteriorating state. Depending on the different temperatures in the tube (Fig. 8(a) and (b)), the heat transfer characteristics can be approximately divided into three regions. As the wall temperature (T_w) is less than T_{pc} near $x/d \approx 50$, the Nusselt number is in keeping with that of the Dittus–Boelter correlation, which is the normal heat transfer. As T_w is greater than T_{pc}, the rising slope of T_w is apparently increased and the heat transfer starts to deteriorate. Notably, the rising slope of T_w becomes gentle suddenly at $x/d \approx 120$, where the first local minimum point of HTD appears correspondingly. While the bulk temperature (T_b) reaches T_{pc} ($H_b \approx H_{pc}$, $x/d \approx 220$), the deterioration starts to recover, generating the second local minimum point of HTD.

The boundary conditions have a great influence on the heat transfer characteristics of supercritical fluids, as learned from the existing experimental study (Xu et al., 2020b). Figure 9 shows the numerical and experimental Nusselt numbers under different heat fluxes and pressures at a mass flux of 500 kg/m^{2}s. The numerical results are basically in agreement with the experimental ones, which can well simulate the heat transfer processes on normal, two deteriorations and recovery. The effects of boundary conditions on the heat transfer characteristics can be concluded that the HTD is more serious with the increase in heat flux and the decrease in supercritical pressure. Furthermore, when the pressure is 2.0 MPa and the heat fluxes are 80 kW/m^2 and 100 kW/m^2, the numerical results are smaller than those of the experiment near the second local minimum point of HTD, and the maximum deviations are 11.7% and 31.9% (Fig. 9(a)). While the pressure is 2.4 MPa and the heat flux is 100 kW/m^2, the maximum deviation of 24.7% appears around the first local minimum point of HTD, and the numerical results are larger than those of the experiment (Fig. 9(b)).

Usually, the characteristics of convective heat transfer in the tube are closely related to the flow state of the fluid. To reveal the mechanism of the deteriorated heat transfer of MM in a vertical upward tube at supercritical pressures and the effects of boundary conditions, the contours of the key information on the turbulent flow in the tube and near the wall are analyzed, and the interactions between the distributions and heat transfer characteristics are discussed in the following.

The distributions of fluid temperature are shown in Fig. 10. In fact, it is a dimensionless temperature defined by the ratio of the local fluid temperature (T_f) to T_{pc} to better distinguish the region that achieved the supercritical

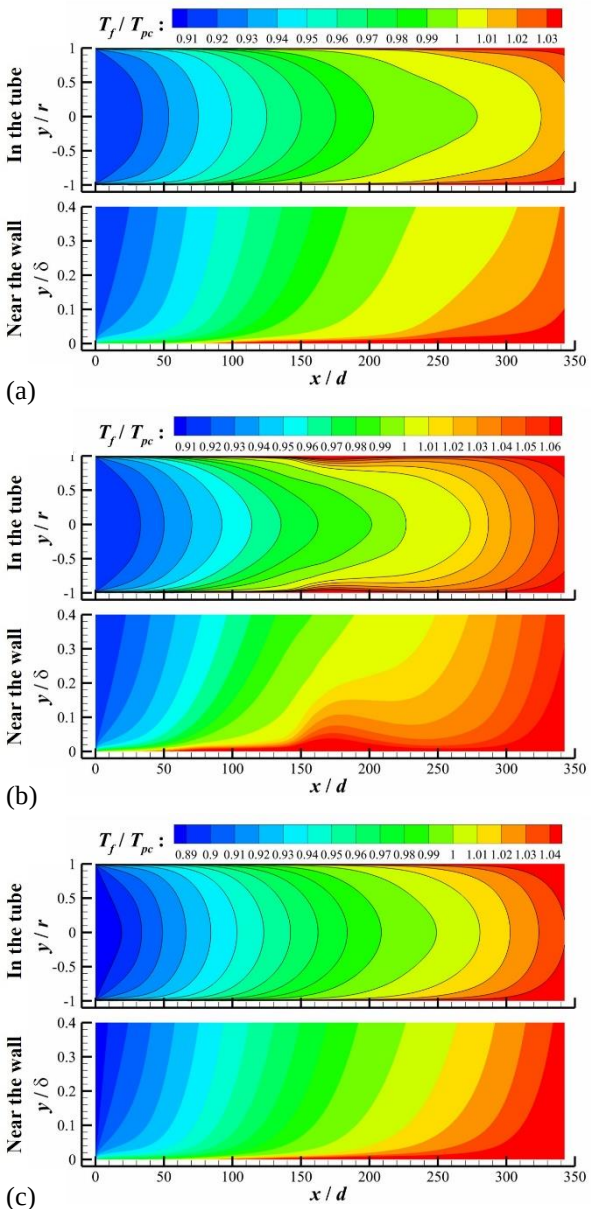

Fig. 10 Contours of distribution on fluid temperature in the tube and near the wall: (a) P = 2.0 MPa, q = 80 kW/m^2; (b) P = 2.0 MPa, q = 100 kW/m^2; (c) P = 2.4 MPa, q = 100 kW/m^2

state. The inlet temperature is 473.15 K. The pseudo-critical temperatures of MM at pressures of 2.0 and 2.4 MPa are 520.55 and 533.02 K, respectively. δ represents the thickness of the flow boundary layer, which is equal to the radius of the tube in the fully developed region. As shown in Fig. 10, on account of the fluid heated by the constant wall heat flux continuously, its trend on distribution is the near-wall temperature is higher than that of mainstream, and the overall gradually increases along the axial direction. Near the contours where the fluid temperature reaches T_{pc}, the gradient of temperature rise decreases noticeably, resulting in the deformation of the temperature profile. When the fluid temperature is completely greater than T_{pc}, the temperature profile gradually returns to normal.

Moreover, by comparing Fig. 10(a) and (b), as the mass flux and pressure are constant and the heat flux increases from 80 kW/m^2 to 100 kW/m^2, a significant high-temperature area appears near the wall ($x/d \approx 140$–200) soon after the fluid temperature is higher than $T_{pc,}$ which may cause the higher thermal resistance and the worse heat transfer. Its temperature profile is severely deformed. While the mass flux and heat flux are constant, the decrease in the gradient of temperature rise in the area near T_{pc} is weakened remarkably with the pressure increased to 2.4 MPa compared with the situation at 2.0 MPa, as shown in Fig. 10(c). It is implied that the tendency of fluid temperature rise in the heating tube will become uniform with the increase in supercritical pressure, and the distribution profile is also changed a little near T_{pc}.

The distributions of fluid density are shown in Fig. 11. The fluid density distribution is inversely proportional to the temperature distribution. The near-wall density is higher than that of mainstream. The fluid density decreases along the axial direction overall, and the

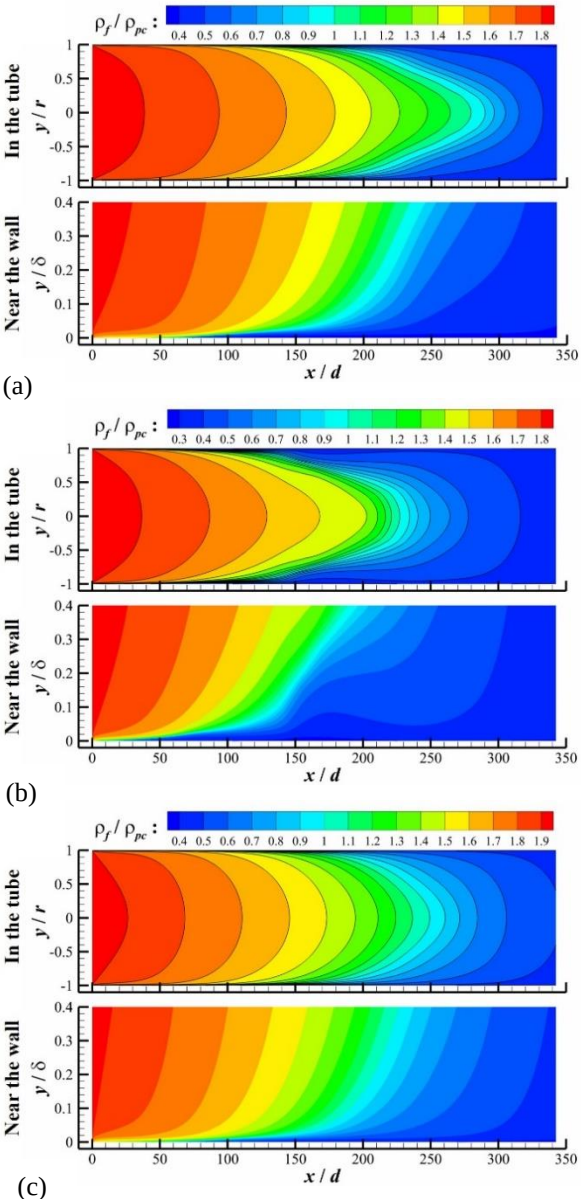

Fig. 11 Contours of distribution on fluid density in the tube and near the wall: (a) P = 2.0 MPa, q = 80 kW/m^2; (b) P = 2.0 MPa, q = 100 kW/m^2; (c) P = 2.4 MPa, q = 100 kW/m^2

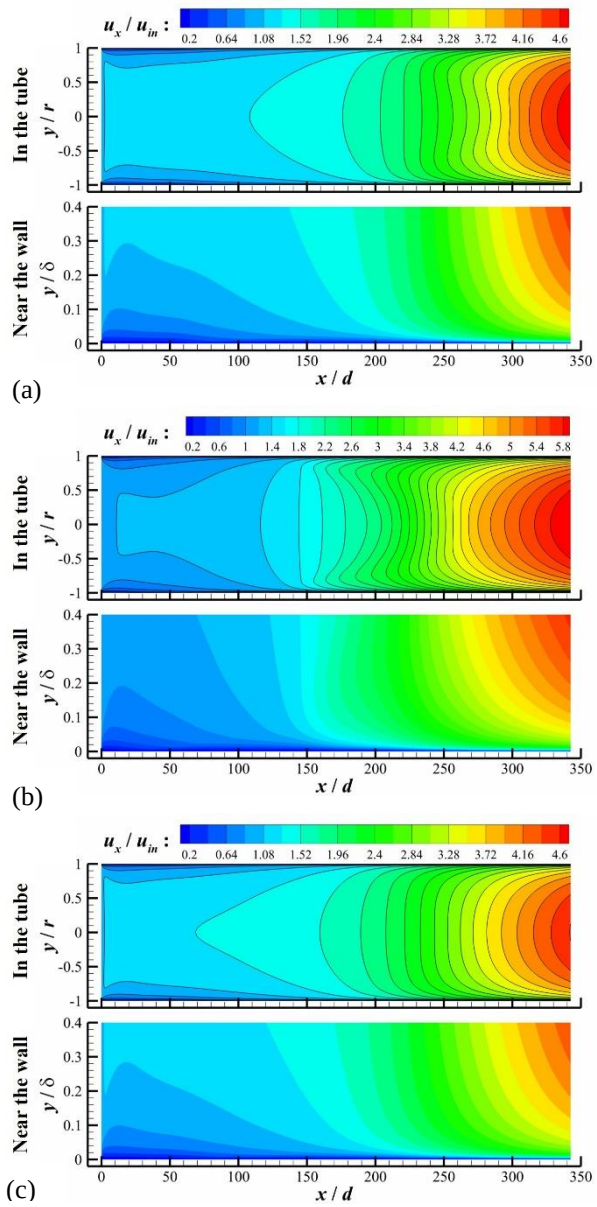

Fig. 12 Contours of distribution on fluid velocity in the tube and near the wall: (a) P = 2.0 MPa, q = 80 kW/m^2; (b) P = 2.0 MPa, q = 100 kW/m^2; (c) P = 2.4 MPa, q = 100 kW/m^2

decreasing gradient is increased near ρ_{pc} significantly, which contributes to the deformation of the density profile.

When the heat flux increases from 80 kW/m^2 to 100 kW/m^2, as shown in Fig. 11(a) and(b), the decreasing gradient of the fluid density near ρ_{pc} is more intensified. While the pressure increases to 2.4 MPa, although the decreasing gradient of the fluid density near ρ_{pc} is increased slightly, as shown in Fig. 11(c), the increasing degree is obviously smaller than that of the pressure of 2.0 MPa. It also indicates that the drastic change of thermal properties of supercritical fluid near the pseudo-critical temperature will be moderated with the increase in supercritical pressure.

Figure 12 shows the distributions of fluid velocity, of which the values are the ratio of the local velocity to the inlet velocity. Since the cross-section of the tube is constant, the fluid velocity will increase with decreasing density. As present in Fig. 12, the fluid velocity increases rapidly after a slow growth from the entrance along the axial direction, and the increasing gradient is intensified, that is, the increasing flow acceleration. The strong flow acceleration would deform the velocity profile, even from U-shaped to M-shaped.

By comparing Fig. 12(a) and (b), it can first be determined that the higher the heat flux is, the faster the flow velocity increases near T_{pc} along the axial direction, which makes the outlet velocity of 100 kW/m^2 higher than that of 80 kW/m^2. Second, it can be seen that the velocity profile with 100 kW/m^2 has more severe deformation than that with 80 kW/m^2, and the M-type velocity distribution is wider. While the pressure increases from 2.0 to 2.4 MPa, as shown in Fig. 12(c), the flow velocity will accelerate for a period near the fluid temperature reaching T_{pc} ($x/d \approx$ 200–250), but it is not as evident as that of 2.0 MPa, and the velocity profile only becomes flattened and does not appear M-shaped.

Figure 13 shows the distributions of flow shear stress. The flow shear stress is defined as follows:

$$\tau = \tau_{lam} + \tau_{tur} = \mu_f \frac{\mathrm{d}u}{\mathrm{d}y} + \mu_{tur} \frac{\mathrm{d}u}{\mathrm{d}y} \tag{12}$$

It is the sum of the local laminar shear stress and turbulent shear stress of the fluid, where μ_f is the dynamic viscosity, μ_{tur} is the turbulent viscosity, namely the eddy viscosity coefficient, and du/dy is the partial derivative of the axial velocity in the radial direction. As shown in Fig. 13, the fluid flow shear stress is lower in the region of entrance and core mainstream, and higher near the wall. Combined with the contours of fluid temperature, it is further observed that the flow shear stress near the wall starts to diminish after the wall temperature reaches T_{pc}. When the local fluid temperature is completely greater than T_{pc}, a minimum flow shear stress region appears in the mainstream area. Subsequently, the flow shear stress near the wall is raised quickly.

Under the condition of 2.0 MPa pressure, as shown in Fig. 13(a) and (b), a pair of symmetric regions with negative shear stress are formed in the mainstream area, whose position corresponds to the velocity profile of M-shaped. The turbulence produced by the fluid in this region should be inhibited, and the turbulence intensity will decrease accordingly. With the increase of heat flux, not only the area of negative shear stress expands, but also its minimum value further decreases. While the pressure is 2.4 MPa, as presented in Fig. 13(c), the mainstream shear stress in the tube will drop to a minimum value, but there is no negative area, which corresponds to whether the fluid velocity distribution appears M-shaped.

The distributions of fluid dimensionless density are shown in Fig. 14. The dimensionless density is defined as $(\rho_b - \rho_f)/\rho_b$, which expresses the comparison values between the local fluid density (ρ_f) and the average density (ρ_b) on the cross section of the tube. Combined with the contours of fluid density, it is learned that the near-wall fluid density starts to decrease sharply after the wall temperature reaches T_{pc}, resulting in $\rho_b > \rho_f$ on the section.

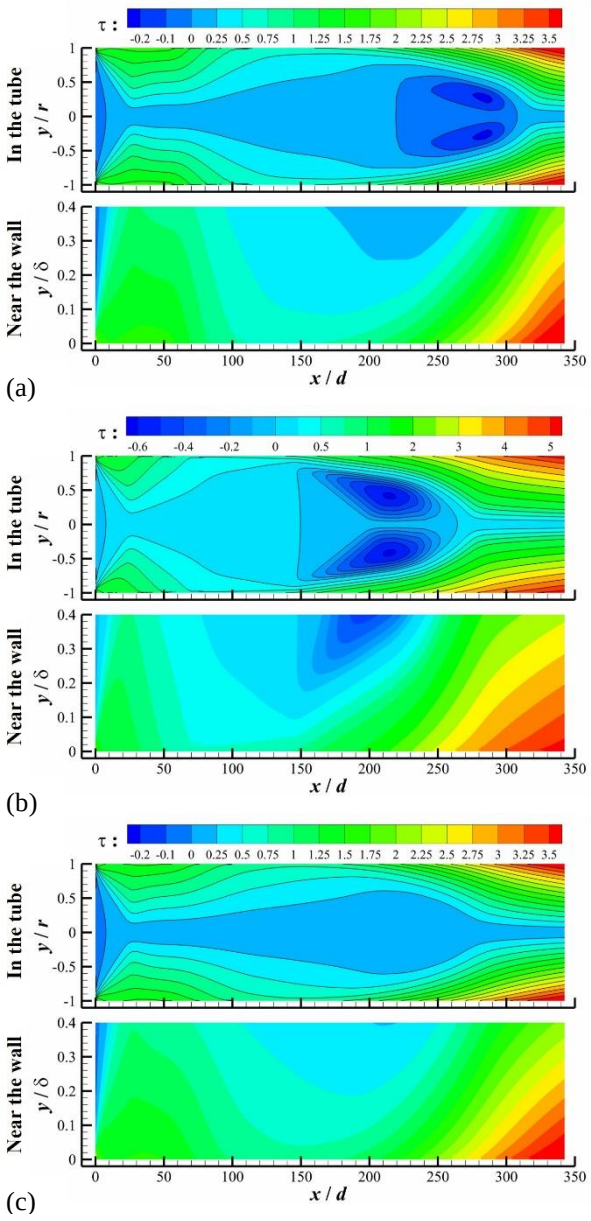

Fig. 13 Contours of distribution on fluid shear stress in the tube and near the wall: (a) *P* = 2.0 MPa, *q* = 80 kW/m^2; (b) *P* = 2.0 MPa, *q* = 100 kW/m^2; (c) *P* = 2.4 MPa, *q* = 100 kW/m^2

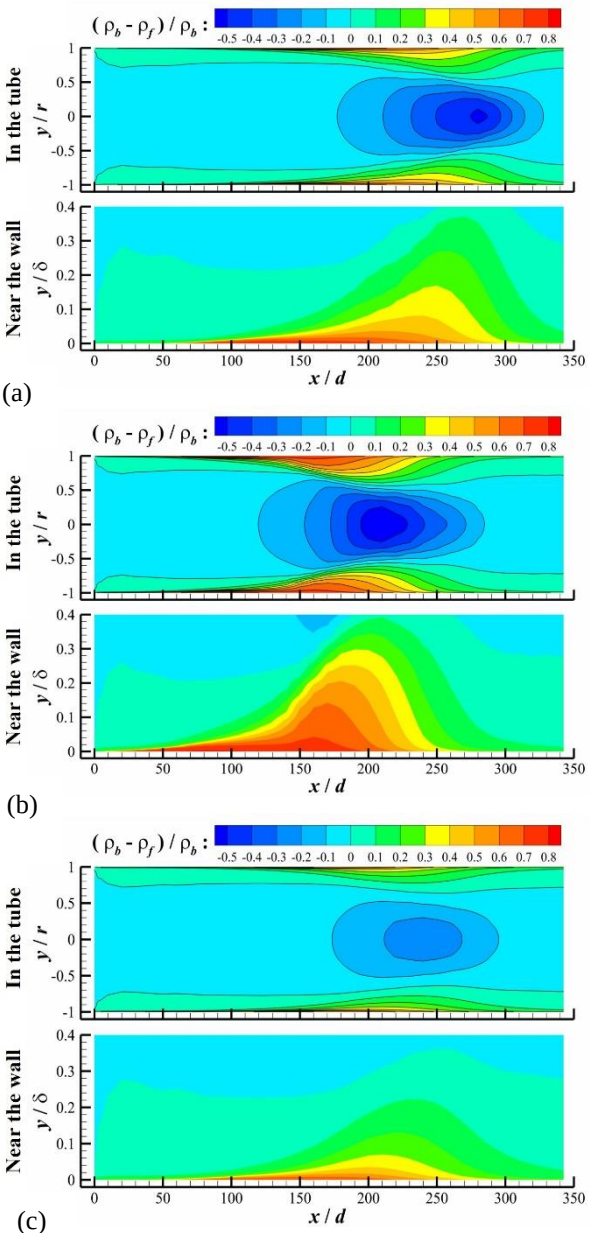

Fig. 14 Contours of distribution on fluid dimensionless density in the tube and near the wall: (a) *P* = 2.0 MPa, *q* = 80 kW/m^2; (b) *P* = 2.0 MPa, *q* = 100 kW/m^2; (c) *P* = 2.4 MPa, *q* = 100 kW/m^2

The radial density difference coupling with gravity will inevitably generate the effect of buoyancy, so the area with positive dimensionless density can represent the region of buoyancy effect, and its strongest region (the red contour line) acts near the wall at $T_w > T_{pc}$. By contrast, when the bulk temperature reaches around T_{pc}, the local fluid density in the mainstream is larger than ρ_b, thus forming a negative dimensionless density area, and the area will first reach a lowest region along the axial direction and then recover. The fluid will be accelerated by the axial reduction of density, so the area with negative dimensionless density can represent the region producing flow acceleration effect, and the strongest region (the blue contour line) is at the same position as the minimum flow shear stress.

Moreover, by comparing Fig. 14(a) and (b), it can be found that increasing the heat flux will magnify the minimum and maximum values of the dimensionless density and their distribution regions. However, increasing the pressure will decrease the absolute values of the extreme ones of the dimensionless density, as well as their distribution regions, as shown in Fig. 14(c). Therefore, it can be implied that the effects of buoyancy and flow acceleration generated by the supercritical heat transfer in the tube will intensify with the higher heat flux and weaken with the higher supercritical pressure.

Figure 15 shows the distributions of fluid turbulence intensity. The turbulence intensity is defined as follows:

$$I = \frac{u'}{\overline{U}} = \frac{\sqrt{\frac{1}{3}\left(u_x'^2 + u_y'^2 + u_z'^2\right)}}{\sqrt{\overline{U}_x^2 + \overline{U}_y^2 + \overline{U}_z^2}} \tag{13}$$

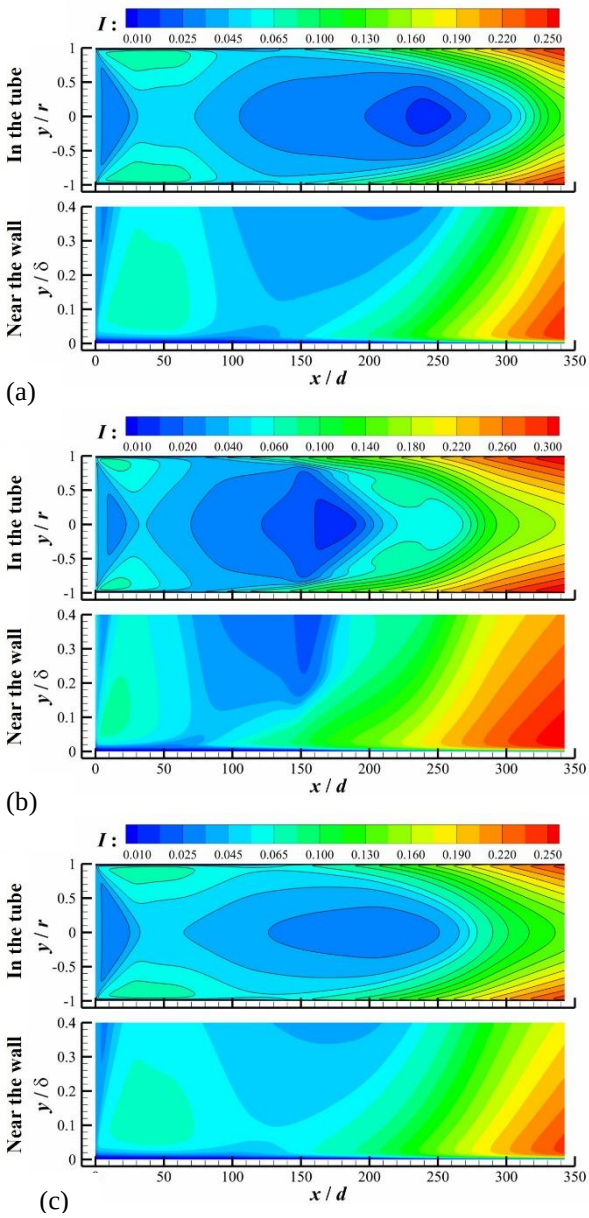

Fig. 15 Contours of distribution on fluid turbulence intensity in the tube and near the wall: (a) P = 2.0 MPa, q = 80 kW/m^2; (b) P = 2.0 MPa, q = 100 kW/m^2; (c) P = 2.4 MPa, q = 100 kW/m^2

which is the ratio of the local root mean square of the turbulent fluctuating velocity to the time-average velocity, and used to represent the level of fluid fluctuation during turbulent flow. As shown in Fig. 15, a near-wall area produces low turbulence intensity and spread to the mainstream after the wall temperature reaches T_{pc}. Based on the contours of dimensionless density, it should be attributed to the strong buoyancy effect. While the bulk temperature reaches T_{pc}, an area with minimal turbulence intensity is created in the mainstream, which may result in local laminarization.

When the heat flux increases from 80 kW/m^2 to 100 kW/m^2, as shown in Fig. 15(a) and (b), although the distribution range of the low turbulence intensity region decreases in the axial direction, its range in the mainstream is expanded significantly in the radial direction. While the pressure increases from 2.0 to 2.4 MPa, as shown in Fig. 15(c), the low turbulence intensity generated near the wall and in the mainstream is alleviated.

On the whole, the heat transfer will deteriorate in the region of $T_b < T_{pc} < T_w$, and there are two local minimum points of HTD. Combined with Fig. 10–15, it is learned that the variation in density in the radial direction near the wall coupling with gravity will form a buoyancy effect in the region of $T_b < T_{pc} < T_w$. The effect of buoyancy can reduce the fluid shear stress and turbulence intensity at the corresponding location, thereby decreasing in heat transfer. Whereas the rapid decline in fluid density in the axial direction will produce a strong effect of flow acceleration near $T_b \approx T_{pc}$, which can deform the profile of fluid velocity and even appear M-shaped, thus reducing the local shear stress and turbulence intensity, ultimately leading to HTD. The positions of two generated sources of low turbulence intensity in Fig. 15 are in good agreement with the locations of two local minimum points of HTD under the same conditions in Fig. 9, so it can be proved that the first HTD is mainly due to the buoyancy effect, and the flow acceleration effect contributes to the second HTD principally. Furthermore, when the heat flux increases, the drop gradient of the fluid density in the tube near T_{pc} will be obviously intensified, resulting in the stronger effects of buoyancy and flow acceleration caused by the density change, and thus more serious HTD. However, the rapid variation in fluid density near T_{pc} will become moderate with the increase in pressure, so the effects of buoyancy and flow acceleration will be weakened, and the HTD will recover.

4. CONCLUSION

The heat transfer characteristics of MM at supercritical pressures in a vertical upward tube are investigated in the present study. Based on the experimental data, the methods of numerical simulation and data processing are first determined. Subsequently, the influences of boundary conditions, including heat flux and pressure, on heat transfer characteristics are discussed. Finally, the mechanism of HTD is revealed by analyzing the distributions of the key turbulent flow parameters under the different conditions. The main conclusions are as follows:

(1) The heat transfer characteristics are HTD, and there is no apparent HTE. The heat transfer starts to deteriorate at $T_w > T_{pc,}$ and recover at $T_b > T_{pc,}$ of which processes will come into being two deteriorated extreme points. The first one is at $T_b < T_{pc} < T_w$, and the second one is near $T_b \approx T_{pc}$.

(2) The buoyancy effect is induced by the drastic variation in fluid density in the radial direction near the wall coupling with gravity in the region of $T_b < T_{pc} < T_w$. By contrast, the flow acceleration effect mainly is caused by the rapid decrease in fluid density in the axial direction near $T_b \approx T_{pc}$. Both of them will reduce the local shear stress and turbulence intensity, thereby inhibiting the heat transfer. The two local minimum points of HTD correspond to the two regions of low turbulence intensity, suggesting that the first HTD is due to the buoyancy effect,

and the flow acceleration effect contributes to the second HTD.

(3) The buoyancy and flow acceleration are enhanced with the increase in heat flux because of the more intense drop gradient of the fluid density near T_{pc}, resulting in more severe HTD. With the increase in supercritical pressure, the effects of buoyancy and flow acceleration are weakened due to the relatively moderate change of fluid density near T_{pc}, thus reducing the deteriorated degree of heat transfer. Therefore, HTD will become more serious with the heat flux increased and recovers with the supercritical pressure raised.

Based on the above conclusions, for the design of SORC system, it is recommended to appropriately increase the inlet pressure of turbine and reduce the heat flux of the heater under the premise of ensuring the stable and efficient operation of the turbine and the overall system, achieving the circumvention of HTD in the heat exchanger to prevent thermal decomposition of the working fluids and reduce the exergy loss of the system.

ACKNOWLEDGEMENTS

We appreciate the support from the National Science and Technology Major Project of China (J2019-III-0021-0065) and the Gansu Youth Science and Technology Fund (23JRRA827).

CONFLICT OF INTEREST

The authors declare that they do not have any commercial or associative interest that represents a conflict of interest in connection with the work submitted. This statement is provided in full compliance with the policies of the Journal of Applied Fluid Mechanics, and the authors take full responsibility for its accuracy.

AUTHORS CONTRIBUTION

Jian Fu: project administration, methodology, investigation, writing—reviewing and editing, funding acquisition. **Hanyi Liu**: software, data curation, writing—original draft preparation. **Yan Wang:** supervision, validation.

REFERENCES

Ackerman, J. W. (1970). Pseudoboiling heat transfer to supercritical pressure water in smooth and ribbed tubes. *Journal of Heat Transfer, 92*(3), 490-497. https://doi.org/10.1115/1.3449698

Cabeza, L. F., De Gracia, A., Fernández, A. I., & Farid, M. M. (2017). Supercritical CO2 as heat transfer fluid: a review. *Applied Thermal Engineering, 125*, 799-810. https://doi.org/10.1016/j.applthermaleng.2017.07.049

Cheng, X., & Schulenberg, T. (2001). Heat transfer at supercritical pressures - literature review and application to an HPLWR. *Forschungszentrum Karlsruhe GmbH*. https://edocs.tib.eu/files/e01fn01/336082746.pdf

Dai, X., Shi, L., & Qian, W. (2019). Thermal stability of hexamethyldisiloxane (MM) as a working fluid for organic Rankine cycle. *International Journal of Energy Research, 43*(2), 896–904. https://doi.org/10.1002/er.4323

Gallarini, S., Spinelli, A., Lietti, L., & Guardone, A. (2023). Thermal stability of linear siloxanes and their mixtures. *Energy, 278*, 127687. https://doi.org/10.1016/j.energy.2023.127687

He, S., Jiang, P. X., Xu, Y. J., Shi, R. F., Kim, W. D., & Jackson, J. D. (2005). A computational study of convection heat transfer to CO2 at supercritical pressures in a vertical mini tube. *International Journal of Thermal Sciences, 44*(6), 521-530. https://doi.org/10.1016/j.ijthermalsci.2004.11.003

Holman, J. P. (2010). *Heat Transfer*. McGraw-Hill Series in Mechanical Engineering. The McGraw-Hill Companies. www.mhhe.com

Hou, J., Zhou, Y., Yuan, Y., & Huang, S. (2024). Numerical study on flow structure and heat transfer of supercritical CO2 in tubes with different inclination angles. *Progress in Nuclear Energy, 168*, 105028. https://doi.org/10.1016/j.pnucene.2023.105028

Huang, D., Wu, Z., Sunden, B., & Li, W. (2016). A brief review on convection heat transfer of fluids at supercritical pressures in tubes and the recent progress. *Applied Energy, 162*, 494-505. https://doi.org/10.1016/j.apenergy.2015.10.080

Jackson, J. D. (2017). Models of heat transfer to fluids at supercritical pressure with influences of buoyancy and acceleration. *Applied Thermal Engineering, 124*, 1481-1491. https://doi.org/10.1016/j.applthermaleng.2017.03.146

Jackson, J. D., Cotton, M. A., & Axcell, B. P. (1989). Studies of mixed convection in vertical tubes. *International Journal of Heat and Fluid Flow, 10*(1), 2-15. https://doi.org/10.1016/0142-727X(89)90049-0

Kim, D. E., & Kim, M. H. (2010). Experimental study of the effects of flow acceleration and buoyancy on heat transfer in a supercritical fluid flow in a circular tube. *Nuclear Engineering and Design, 240*(10), 3336-3349. https://doi.org/10.1016/j.nucengdes.2010.07.002

Kim, D. E., & Kim, M. H. (2011). Experimental investigation of heat transfer in vertical upward and downward supercritical co2 flow in a circular tube. *International Journal of Heat and Fluid Flow, 32*(1), 176-191. https://doi.org/10.1016/j.ijheatfluidflow.2010.09.001

Lai, N. A., Wendland, M., & Fischer, J. (2011). Working fluids for high-temperature organic rankine cycles. *Energy, 36*(1), 199-211. https://doi.org/10.1016/j.energy.2010.10.051

Lecompte, S., Huisseune, H., Martijn, V. D. B., Vanslambrouck, B., & De Paepe, M. (2015). Review of organic rankine cycle (orc) architectures for waste heat recovery. *Renewable & Sustainable Energy Reviews, 47*(jul), 448-461.

https://doi.org/10.1016/j.rser.2015.03.089

Lei, X., Li, H., & Zhang, W. (2016). Numerical analysis on heat transfer deterioration of supercritical fluid in the vertical upward tubes. *Journal of Nuclear Engineering and Radiation Science*, *2*(3), 031017. https://doi.org/10.1115/1.4032872

Li, N., Pu, H., Zhou, L., Qu, H., Zhang, Y., & Dong, M. (2024). Numerical analysis of mixed convection phenomena in heat transfer to supercritical pressure carbon dioxide inside a horizontal miniature tube. *Applied Thermal Engineering*, *237*, 121753. https://doi.org/10.1016/j.applthermaleng.2023.121753

Liu, M., Zhang, Z., Yang, X., Tu, J., & Jiang, S. (2023). Numerical study on heat transfer characteristics of supercritical water in straight and helical tubes. *Applied Thermal Engineering*, *226*, 120276. https://doi.org/10.1016/j.applthermaleng.2023.120276

Liu, S., Huang, Y., Liu, G., Wang, J., & Leung, L. K. H. (2017). Improvement of buoyancy and acceleration parameters for forced and mixed convective heat transfer to supercritical fluids flowing in vertical tubes. *International Journal of Heat and Mass Transfer*, *106*, 1144-1156. https://doi.org/10.1016/j.ijheatmasstransfer.2016.10.093

Loni, R., Najafi, G., Bellos, E., Rajaee, F., & Mazlan, M. (2020). A review of industrial waste heat recovery system for power generation with organic rankine cycle: recent challenges and future outlook. *Journal of Cleaner Production*, *287*, 125070. https://doi.org/10.1016/j.jclepro.2020.125070

Mao, S., Zhou, T., Wei, D., Liu, W., & Zhang, Y. (2021). Heat transfer characteristics of supercritical water in channels A systematic literature review of 20 years of research. *Applied Thermal Engineering*, *197*, 117403. https://doi.org/10.1016/j.applthermaleng.2021.117403

Mceligot, D. M., Coon, C. W., & Perkins, H. C. (1970). Relaminarization in tubes. *International Journal of Heat and Mass Transfer*, *13*(2), 431-433. https://doi.org/10.1016/0017-9310(70)90118-3

Menter, F. R. (1994). Two-equation eddy-viscosity turbulence models for engineering applications. *AIAA Journal*, *32*, 1598-1605. https://doi.org/10.2514/3.12149

Mikielewicz, D. P., Shehata, A. M., Jackson, J. D., & Mceligot, D. M. (2002). Temperature, velocity and mean turbulence structure in strongly heated internal gas flows: comparison of numerical predictions with data. *International Journal of Heat and Mass Transfer*, *45*(21), 4333-4352. https://doi.org/10.1016/S0017-9310(02)00119-9

Mohseni, M., & Bazargan, M. (2012). A new analysis of heat transfer deterioration on basis of turbulent viscosity variations of supercritical fluids. *Journal of Heat Transfer*, *134*(12), 1-7. https://doi.org/10.1115/1.4007313

Nieuwenhuyse, J. V., Lecompte, S., & Paepe, M. D. (2023). Current status of the thermohydraulic behavior of supercritical refrigerants: a review. *Applied Thermal Engineering*, *218*, 119201. https://doi.org/10.1016/j.applthermaleng.2022.119201

Pioro, I. L. (2019). Current status of research on heat transfer in forced convection of fluids at supercritical pressures. *Nuclear Engineering and Design*, *354*, 110207. https://doi.org/10.1016/j.nucengdes.2019.110207

Pizzarelli, M. (2018). The status of the research on the heat transfer deterioration in supercritical fluids: a review. I*nternational Communications in Heat and Mass Transfer*, *95*, 132-138. https://doi.org/10.1016/j.icheatmasstransfer.2018.04.006

Tu, Y., & Zeng, Y. (2021). Heat transfer and hydraulic characteristics of supercritical CO2 in cooled and heated horizontal semicircular channels. *Journal of Applied Fluid Mechanics*, *14*(5), 1351–1362. https://doi.org/10.47176/jafm.14.05.32163

Wang, W., Dai, X., & Shi, L. (2022). Influence of thermal stability on organic rankine cycle systems using siloxanes as working fluids. *Applied Thermal Engineering*, *200*, 117639. https://doi.org/10.1016/j.applthermaleng.2021.117639

Xu, J., Zhang, H., Zhu, B., & Xie, J. (2020a). Critical supercritical-boiling-number to determine the onset of heat transfer deterioration for supercritical fluids. *Solar Energy*, *195*, 27-36. https://doi.org/10.1016/j.solener.2019.11.036

Xu, G., Fu, J., Quan, Y., Wen, J., & Dong, B. (2020b). Experimental investigation on heat transfer characteristics of hexamethyldisiloxane (mm) at supercritical pressures for medium/high temperature orc applications. *International Journal of Heat and Mass Transfer*, *156*, 119852. https://doi.org/10.1016/j.ijheatmasstransfer.2020.119852

Xu, G., Ju, Y., Gao, W., Fu, J., & Dong, B. (2022). Experimental and numerical investigation of the effects of buoyancy and flow acceleration on the heat transfer of hexamethyldisiloxane (mm) at supercritical pressures. *International Journal of Heat and Mass Transfer*, 187, 122581. https://doi.org/10.1016/j.ijheatmasstransfer.2022.122581

Yağli, H., Koç, Y., Koç, A., Gorgülü, A., & Tandiroğlu, A. (2016). Parametric optimization and exergetic analysis comparison of subcritical and supercritical organic rankine cycle (orc) for biogas fuelled combined heat and power (chp) engine exhaust gas waste heat. *Energy*, *111*, 923-932. https://doi.org/10.1016/j.energy.2016.05.119

Yang, Z., Bi, Q., Liu, Z., Guo, Y., & Yan, J. (2015). Heat transfer to supercritical pressure hydrocarbons flowing in a horizontal short tube. *Experimental Thermal and Fluid Science*, *61*, 144-152. https://doi.org/10.1016/j.expthermflusci.2014.10.024

Yoo, J. Y. (2013). The turbulent flows of supercritical fluids with heat transfer. A*nnual Review of Fluid Mechanics*, *45*(1), 495-525. https://doi.org/10.1146/annurev-fluid-120710-101234

Zhu, B., Xu, J., Yan, C., & Xie, J. (2020). The general supercritical heat transfer correlation for vertical up-flow tubes: k number correlation. *International Journal of Heat and Mass Transfer, 148*(8), 119080. https://doi.org/10.1016/j.ijheatmasstransfer.2019.119080

Zhu, J., Zhao, C., Cheng, Z., Lin, D., Tao, Z., & Qiu, L. (2019). Experimental investigation on heat transfer of n-decane in a vertical square tube under supercritical pressure. *International Journal of Heat & Mass Transfer*, *138*(AUG.), 631-639. https://doi.org/10.1016/j.ijheatmasstransfer.2019.04.076